Influence of RF excitation during PLD in oxygen atmosphere on the structural properties and luminescence of nano-crystalline ZnO:Al thin films

Daniel Meljanac[a),1], Krunoslav Juraić[1,2], Milivoj Plodinec[1],Zdravko Siketić[1], Davor Gracin[1]

[1]Ruđer Bošković Institute, Bijenička 54, 10000 Zagreb, Croatia

[2]Institute of Inorganic Chemistry, Graz University of Technology, Stremayrgasse 9/IV, 8010 Graz, Austria

Nikša Krstulović, Krešimir Salamon, Hrvoje Skenderović, Zlatko Kregar, Iva Šrut Rakić

Institute of Physics, Bijenička 46, 10000 Zagreb, Croatia

Sigrid Bernstorff

Elettra-Sincrotrone Trieste, SS 14, Km 163.5, I-34049Basovizza (TS), Italy

[a)] Electronic mail: dmeljan@irb.hr

Thin ZnO:Al layers were deposited by pulsed laser deposition (PLD) in vacuum and in oxygen atmosphere at gas pressures between 10 and 70 Pa and by applying RF plasma. Grazing incidence small angle x-ray scattering (GISAXS) and grazing incidence x-ray diffraction (GIXRD) data showed that an increase of the oxygen pressure leads to an increase of the roughness, a decrease of the sample density and to changes in the size distribution of nano-voids. The nano-crystals sizes estimated from GIXRD were around 20 nm, while the sizes of the nano-voids increased from 1 to 2 nm with the oxygen pressure. The RF plasma mainly influenced the nano-structural properties and point defects dynamics. The photoluminescence consisted of 3 contributions: UV, blue emission due to Zn vacancies, and red emission which is related to an excess of oxygen. The RF excitation lowered the defect level related to blue emission and narrowed the UV luminescence peak, which indicates an improvement of the structural ordering. The

observed influence of the deposition conditions on the film properties is discussed as a consequence of two main effects: the variation of the energy transfer from the laser plume to the growing film, and changes in the growth chemistry.

I. INTRODUCTION

Zinc oxide is a material which is suitable for many applications due to the large band gap (3.37 eV), the high carrier mobility and the relatively high exciton binding energy (60 meV). Furthermore, the synthesis is easy and the material is not toxic. The combination of high conductivity and transparency for visible light makes this material a possible candidate for front electrodes in thin film solar cells. An additional advantage for this application comes from the possibility to produce ZnO in a variety of nano structural forms with large actual to nominal surface ratio[1]. The luminescence in the UV, blue, green, yellow and red makes ZnO interesting also for various applications in optical devices and optoelectronics[2-7]. When ZnO has a high surface-to-volume ratio at the nanometre scale, its surface defects play an important role for the properties, which often give rise to interesting phenomena[6].

ZnO can be deposited in many ways using chemical and physical techniques. Although the growth and properties of ZnO nanostructures have been extensively studied, there are still a number of unanswered questions concerning the relationship between the details of the fabrication conditions and the optical properties[8]. Among other methods, pulsed laser deposition (PLD) attracts recently considerable attention due to the possibility of preserving the stoichiometry of the target and due to the relatively simple set-up for the production of multi-component and multilayer structures. The deposition can be done in vacuum or in reactive or inert atmosphere independently of the sputtering process. There are many parameters that can be varied during deposition, like laser wavelength, laser power, target to substrate distance, temperature and type of substrate, and others[9-15]. The influence of the oxygen pressure on the structural and optical properties of ZnO deposited by PLD in neutral oxygen atmosphere on heated substrate was studied by several authors[16,17]. They found that deposition in O_2 atmosphere results

in a change of the Zn/O ratio in favor of oxygen. Consequently, the stress changed from compression to tensile type, the concentration of oxygen vacancies decreased, the grain size increased, while the crystal sizes remained the same. Most of their samples were deposited at elevated temperatures (between 400 and 700°C), which resulted in well-ordered samples with a low level of point defects. Generally, a high substrate temperature yields samples with a low level of defects.

In this study we explore the possibility to modify the structure and luminescence properties of ZnO thin films by changing the reactivity of the oxygen atmosphere in the depositing chamber by adding RF plasma at various pressures[18, 19]. The geometry of the experiment was chosen in such a way that only active oxygen species could influence the film growth (Figure 1). The deposition was performed at room temperature, expecting that the influence of the reactive atmosphere will be more evident then. The obtained nano structural changes were analyzed by x-ray scattering at grazing incidence angles, while the surface structures were monitored by microscopy. Information about the point defects dynamic was obtained by luminescence measurements.

II. EXPERIMENTAL

A. *Preparation of samples*

The experimental setup is composed of two parts; a radio-frequency inductively coupled plasma (RF-ICP) vessel and a pulsed laser deposition (PLD) chamber, which are interconnected as shown in Figure 1.
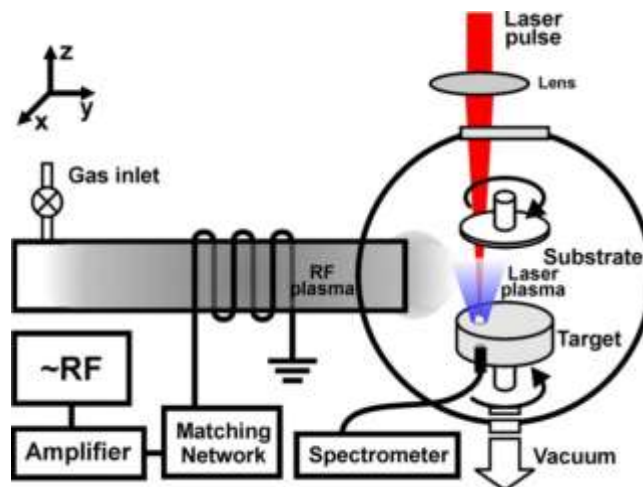
FIG. 1. (Color online) Experimental set-up for film deposition.

The discharge vessel was a linear tube with an outer diameter of 4 cm made of borosilicate glass. The tube was connected to the PLD chamber, which was evacuated using a rotary pump with a pumping speed of $35 m^3 h^{-1}$ and a base pressure of < 1 Pa. The total pressure of the oxygen gas in the system was measured with a Baratron gauge. During the deposition in oxygen, a constant flow of pure oxygen was applied in order to ensure a high purity of the working gas. Plasma was created within an 8 turn coil (total length: 1cm) connected through a matching network to a RF amplifier (RIZ SW Amplifier). The amplifier was fed by oscillation from a frequency generator (Hameg HM8131-2) at a frequency of 13.56 MHz. The discharge power was adjustable up to 300 W. The forward and reflected power components were monitored at the amplifier and optimized at the matching network. The coil was placed at a distance of 5 cm from the edge of the glass tube (i.e. 3 cm from the PLD chamber). The plasma was monitored by an optical spectrometer in order to control its content.

Catalytic probes were used to measure the concentration of neutral oxygen atoms in the RF plasma. The probes were positioned between the target and the substrate. More details on catalytic probe measurements can be found in[20]. The measured concentrations of neutral oxygen atoms at different pressures are: $(4.2\pm0.2)\cdot10^{14} cm^{-3}$ for 10 Pa of RF oxygen plasma, $(3.9\pm0.2)\cdot10^{14} cm^{-3}$ for 30 Pa of RF oxygen plasma and $(2.6\pm0.1)\cdot10^{14} cm^{-3}$ for 70 Pa of RF oxygen plasma.

PLD was performed using a Nd:YAG laser operating at 1064 nm and with 5 Hz repetition rate. The duration of a laser pulse was 4 ns, while the output energy was 300 mJ giving a fluence of 15 J/cm^2 after focusing onto the target surface. The distance between target and substrate was 3 cm. The target surface was parallel to the substrate and inclined by 45° with respect to the impinging laser pulse (the normal of the target surface was inclined by 45° in the x-z plane, while the laser pulse travelled in –z direction as depicted in Figure 1). Both the target holder and substrate were kept on floating potential and at room temperature during deposition and were rotated to avoid drilling of the target, and to increase the homogeneity of the deposited films. The target was ceramic ZnO with an addition of 3% of Al. Each film was deposited using 2000 laser pulses either

in vacuum, in oxygen, or in oxygen RF plasma atmospheres of 10, 30 and 70 Pa, respectively, on quartz glass and silicon substrate.

When the RF plasma is turned on during PLD, the optically most intense part of the plasma is within the coil. However, the plasma is spread in y direction, thus delivering reactive oxygen atoms in the space between target and substrate. The density of reactive oxygen decreases with increasing pressure (and with the distance from the coil).

B.   Structural measurements

The deposited films were structurally examined with grazing incidence X-ray diffraction (GIXRD), specular X-ray reflectivity (XRR) and grazing incidence X-ray scattering (GISAXS). For the first two experiments the same diffractometer was used, equipped with a Co X-ray tube and a W/C multilayer for beam monochromatization. GISAXS was performed at the SAXS beamline of the synchrotron Elettra, Trieste, Italy. In all experiments, the grazing geometry was used in order to enhance the irradiation and diffraction yield of the relatively thin ZnO films. GIXRD for all samples was performed at a fixed grazing incidence angle of α_i=0.45°, slightly above the critical angle of total reflection, α_{crit}, for ZnO and Co Kα radiation. At this angle, the penetration depth of the X-rays perpendicular to the film surface covers a film thickness of approximately 100 nm. The diffracted spectra were collected with a curved position sensitive detector (RADICON) in the angular range 2Theta=30°-85°. XRR spectra were collected by determining the intensity of the specular reflection from the film surface as a function of the incidence angle α_i. A linear detector (Hecus PSD-50M), placed 500 mm from the sample, enabled a resolution step of 0.003° and an angular range $2\theta = 0°-4°$. An aluminum attenuator was used in front of the detector to avoid its damage or saturation, which allowed for a dynamical scale of six orders of magnitude. The reflectivity measurements were used to determine the thickness and the roughness of the ZnO films.

The GISAXS experiment was done at the Austrian SAXS beamline at the Elettra Synchrotron by using an 8 keV X-ray beam[21]. The beam size was 2mm x 200 μm (horizontal x vertical), and the sample to detector distance was L=1980 mm. 2D GISAXS

patterns were recorded with a Pilatus3 1M detector (981 x 1043 pixel array, 172x172µm^2 pixel size) for grazing angles of incidence in the range near the critical angle for total external reflection characteristic for ZnO (at α_c~0.33^o and α_c+0.02^o). The corresponding attenuation lengths are in the range from 10-20 nanometers for α_c and some 50 nm for α_c+0.02^o. Silverbehenate powder was used as calibrant to determine the sample to detector distance, direct beam position and the detector horizontal and vertical tilt angles.

C. *Photoluminescence setup*

Photoluminescence (PL) measurements were performed with the fourth harmonic of a pulsed Nd:YLF laser at 1kHz repetition rate and 100 ns pulse duration. The laser beam at the fourth harmonic with a wavelength of 263 nm and an average power of 10 mW was mildly focused onto the sample resulting in a 100 µm diameter spot, which was imaged onto the entrance slit of a spectrograph (Shamrock 303i). After dispersion on a 150 grooves/mm grating the PL spectra were recorded by a thermoelectrically cooled CCD camera (Andori Dus). Each PL spectrum was taken with 1s exposure time, and then averaged over 10 exposures.

D. *Microscopy*

The AFM measurements were performed with a Flex AFM (Nanosurf) in tapping mode with a set point of 55%. AFM tips of type App Nano (ACLA-10) were used with a force constant of 58 N/m, a frequency of 190 kHz and a tip radius of curvature < 10 nm. All of the AFM data analysis was performed with the WSxM software[22].

The surface morphologies of the samples were obtained on a field-emission-gun scanning electron microscope, FE-SEM (JEOL 7610F). The measurements were performed with an acceleration voltage between 5 – 15 kV and the imaging modes LEI and SEI.

III. RESULTSAND DISCUSSION

A. *Film composition*

The film composition was measured by time of flight elastic recoil detection analysis, TOF ERDA[23]. The results of the measurements are given in Table I. For all samples, except for the sample deposited under vacuum, the number of oxygen atoms is larger than the sum of the Zn and Al atoms. This could be explained either by oxygen interstitial atoms or Zn vacancies. There is some amount of carbon atoms on the surface of the films when films were exposed to ambient atmosphere, even for a short time. The number of carbon atoms increases with the roughness (Table II), implying that such structure is favorable for gas sensing devices. The sample density is estimated by dividing the total amount of atoms per unit area and the film thickness, as determined from the XRR measurement (Tab II)[24], assuming homogeneous growth.

Table I. Composition of deposited ZnO films calculated from TOF ERDA results.

| Sample	Thickness $[10^{15}at/cm^2]$	Density $[g/cm^3]$	(Zn+Al)/O	O $[10^{15}at/cm^2]$	Al $[10^{15}at/cm^2]$	Zn $[10^{15}at/cm^2]$	H $[10^{15}at/cm^2]$	C $[10^{15}at/cm^2]$
vacuum	820	6.07	1.00	410±25	20±2	390±20	30	2
10 Pa O_2	1050	5.40	0.93	530±30	17±2	475±20	26	3
10 Pa O_2/RF	1060	5.04	0.98	520±30	16±2	490±20	20	2
30 Pa O_2	660	5.44	0.93	320±20	10±2	290±15	37	5
30 Pa O_2/RF	840	5.17	0.94	410±25	16±2	370±15	30	6
70 Pa O_2	1460		0.92	700±40	29±2	620±20	102	5
70 Pa O_2/RF	1700		0.91	850±50	37±2	760±30	48	9

B. Structure

1. GIXRD
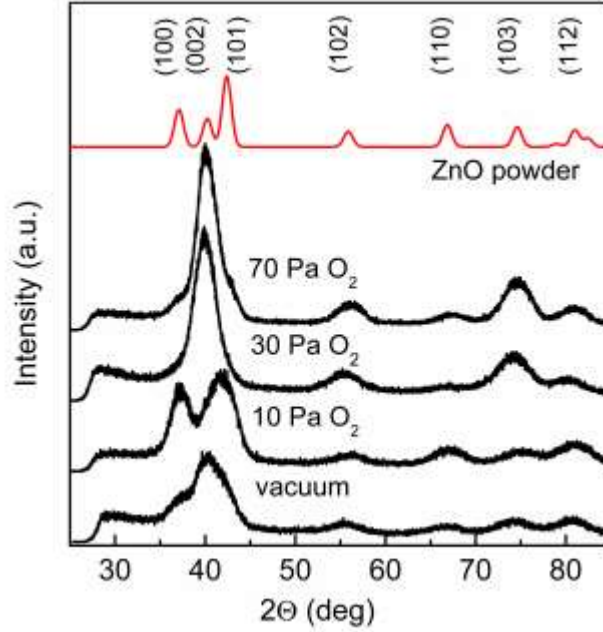
FIG. 2. (Color online) GIXRD curves for ZnO thin films deposited under vacuum and under various O_2 pressures. On top is shown the simulated diffraction of wurtzite ZnO powder.

Figure 2 shows the GIXRD spectra of ZnO films deposited under various O_2 pressures, and also of a film deposited under vacuum condition. For comparison, the simulated diffraction of wurtzite ZnO powder is shown above the experimental curves. The peaks are considerably broadened due to the grazing geometry and small crystallite sizes. Thus, some of the peaks, very close in 2θ, are overlapping and thus are hard to resolve. Nevertheless, the peaks positions in the experimental curves match well with those of ZnO powder. However, the altered intensity ratios of the measured Bragg peaks indicate a preferred orientation of the ZnO crystallites. A determination of the type and degree of the texture from GIXRD is not straightforward since each diffraction peak in grazing incidence geometry corresponds to a different orientation of the reflecting planes with respect to the sample's surface. As shown in Fig. 2, the dominant peaks in the GIXRD curves of the 30 and 70 Pa films are the (002) and (103) reflections, while the (100) and (101) reflections are hardly resolvable. This indicates that the *c*-axis of most of the ZnO crystallites in these films is aligned within some ±15°from the film surface normal. In particular, the angle between the (103) planes and the surface in the (001)

8

texture is 31.65°, which is close (within ~5°) to the Bragg condition for the (103) reflection in grazing geometry. The degree of the (001) texture is a crude estimation and can be correctly determined only with (001) pole figure measurements. The *a*-axis is distributed randomly in the film surface as GIXRD shows no changes when rotating the samples around the surface normal. The film deposited under vacuum conditions exhibits a weaker preference to (001) texture as compared to films deposited under 30 and 70 Pa O_2. On the other hand, the intensity ratios of the peaks in the GIXRD of the film deposited under 10 Pa O_2 RF indicate randomly oriented or only weakly ordered ZnO crystallites. For a given oxygen pressure, the GIXRD curves for films deposited in oxygen atmosphere with and without RF plasma are almost identical.

The average sizes of the ZnO crystallites, estimated using the Scherrer equation and the width at half maximum height of the given GIXRD peaks, after correction for instrumental and grazing geometry broadening, were (20 ±5) nm for all films.

2. XRR

The experimental XRR curves are plotted in Figure 3 together with the corresponding simulations (full lines); the corresponding O_2 conditions are indicated in the figure. Firstly, except for the films deposited with 70 Pa, the XRR curves are characterized by fringes due to the uniform thickness of the ZnO films. Additionally, we observed a long wavelength modulation of the XRR intensity, which corresponds to a very thin surface layer with different density that is possibly due to surface contamination with carbon atoms. The densities of the ZnO films, determined from the critical angles[25], were ~3 – 6% lower than the bulk density of ZnO. The small deficiency in the density can be assigned to the presence of either nano-voids or atomic vacancies in the ZnO crystallites. We further note that the XRR curves for films deposited under the same O_2 pressure and with or without RF plasma in the deposition chamber are qualitatively similar and recall that the same pair-similarity was also found in the GIXRD results. The XRR data were simulated using Parratt's recursion-relation formalism[26]. The effect of the roughness was taken into account by reducing the Fresnel reflection amplitude at each interface by a factor exponentially dependent on the interface roughness σ [27]. In the

modelling of the experimental data, we added at the top of the ZnO film a very thin layer with reduced density. This significantly improved the quality of the fits. The main parameters – thickness and surface roughness of the ZnO films – obtained by the best fitting are reported in Table II. The second layer, which was added at the top of the film was very thin (~3-5 nm), consisting probably of the carbon atoms seen by ERDA (Table I).
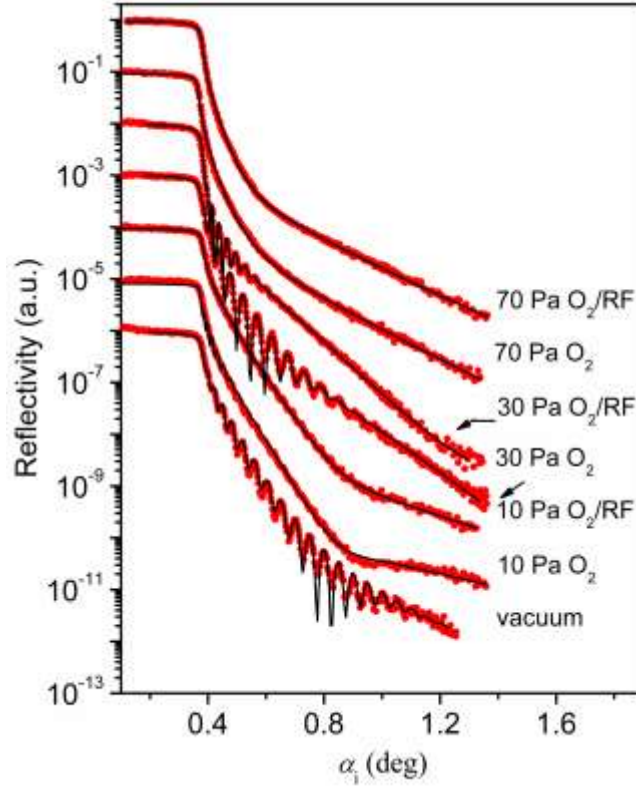

FIG. 3. (Color online) XRR spectra for all studied ZnO thin films deposited under different O_2 atmosphere, together with the corresponding fits (full lines). The curves are vertically shifted for clarity.

Table II. Morphological parameters of the ZnO films as obtained after fitting the Parratt model to the XRR curves.

Sample	Thickness (nm)	RMS Roughness (nm)
vacuum	91	1.5
10 Pa O_2	128	2.4
10 Pa O_2/RF	138	2.5
30 Pa O_2	77	3.0
30 Pa O_2/RF	105	3.5
70 Pa O_2	/	7.5
70 Pa O_2/RF	/	7.1

For the two films deposited with 70 Pa the fringes are irresolvable and thus a determinations of their thicknesses from the fittings was unreliable. The reason for this is the relatively large surface roughness obtained from the fit, which also might reflect a non-uniformity in the average density profile across the surface normal. From Table II, it is evident that the surface roughness increases with the oxygen pressure.

We also note that the films deposited under the same pressure exhibit different thicknesses: RF plasma yields slightly thicker films as can be seen from Tables I and II.

3. GISAXS

The GISAXS pattern are plotted in Figure 4 for samples deposited in vacuum and under various oxygen pressures, with or without RF excitation, for a grazing incidence angle equal to the critical angle, α_{crit}, which corresponds to a penetration depth of some 10-20 nm into the samples. On the axis are the Q vector components parallel to sample surface (Q_y) and normal to the sample surface (Q_z), respectively. The intensity is represented by colors and the log scale is given on the right side of each of the Figures 4a-f. The wide black bar in the middle of the pattern is a partly transparent beam stop, while the thinner horizontal and vertical black lines are dead areas of the detector. The patterns qualitatively follow the results obtained for the roughness obtained by XRR. The 2D GISAXS patterns show strong scattering in the specular plane ($Q_y=0$) for all samples, with additional off-specular diffuse scattering ($Q_y>0$) mainly from the sample surface roughness or voids. The intensity gradient is related to the particles size – faster changes correspond to larger particles. For vacuum condition (Figure 4a) it is evident that the particles are larger in the direction parallel to the surface than perpendicular to it. As the roughness increases, going from Figure 4a to 4d, the patterns are more symmetrical, suggesting similar sizes in both directions. The influence of the RF excitation at a defined gas pressure reflects itself in a less rounded spectrum and somewhat larger particles, as seen by comparing Figures 4c and 4d, as well as 4e and 4f. The above mentioned characteristics of the GISAXS pattern can be better seen in vertical (Figure 5) and horizontal 1D-cuts (not shown here).
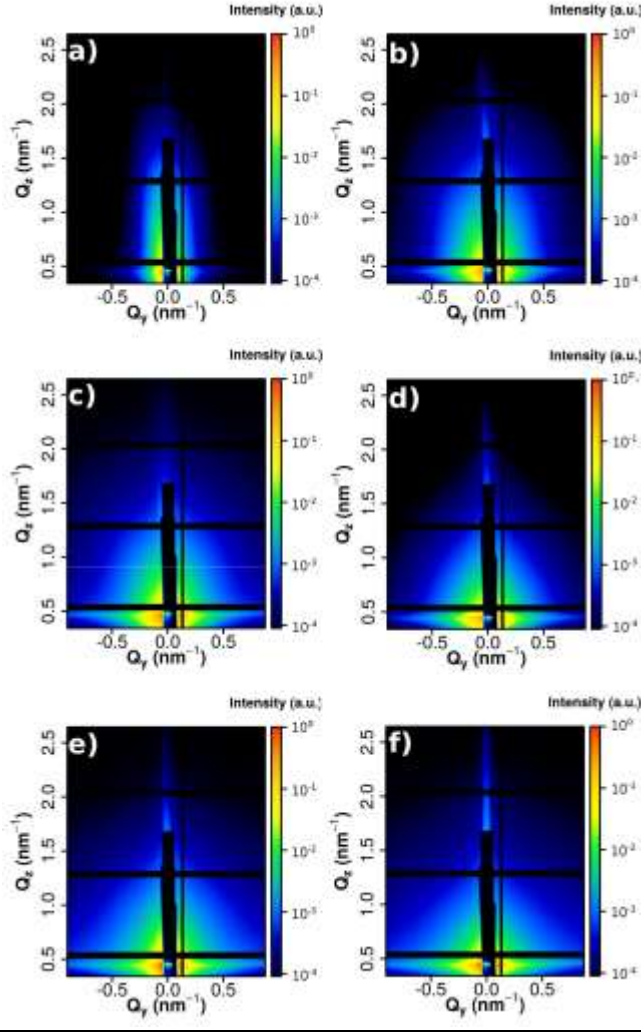
FIG. 4. (Color online) GISAXS patterns obtained at a grazing incidence angle equal to the critical angle, for samples deposited under various oxygen pressures and RF excitations: a) vacuum; b) 10Pa O2 RF; c) 30Pa O2; d) 30Pa O2 RF; e) 70Pa O2; f) 70Pa O2 RF.

The intensive GISAXS signal suggests the presence of nano-sized objects in layers with a different electron density. The analysis was done for a grazing incidence angle of 0.02^0 above the critical angle, which corresponds to a penetration depth of some 50 nm below the surface of the samples. (The estimated thickness of the films was between 80 and 150 nm). Intensity cuts in the direction perpendicular to the sample surface ($Q_y = 0$, corresponding to the beam stop area) were used to precisely determine the grazing angle of incidence by fitting the specular reflected intensity maximum to a Gaussian peak profile function. For the quantitative analysis of the surface morphology,

we used 1D intensity cuts taken in a slightly off specular plane ($Q_y = 0.113$ nm^{-1}) in order to avoid the detector area covered by the Al beamstop (Figure 5), and lateral cuts (parallel to the sample surface) at the position of the Yoneda maximum.
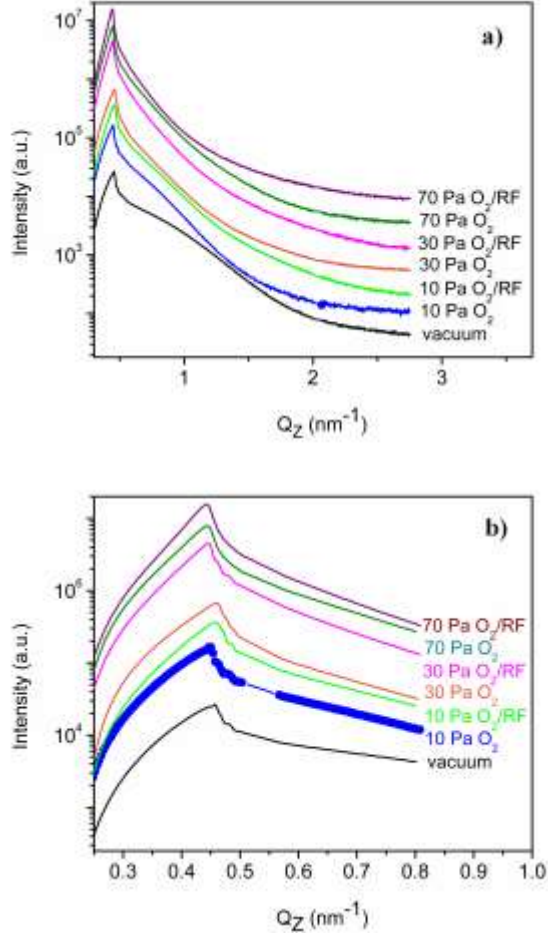

FIG. 5. (Color online) a) Intensity cuts taken in the direction perpendicular to the sample surface close to the specular plane ($Q_y = 0.113$ nm) for the grazing angle of incidence $\alpha_i = \alpha_c + 0.02°$ for samples deposited under various deposition conditions; b) magnified part around the Yoneda peak.

The fitting model for the intensity near the Yoneda maximum can be described within the Distorted Wave Born Approximation by the expression[28]:

$$I(Q) = I_0 + I_f |t(k_i)|^2 |t(k_f)|^2 S_H(Q),\qquad \text{(eq. 1)}$$

where I_0 is the background intensity, I_f is the intensity scaling factor, $t(k_i)$ and $t(k_f)$ are the Fresnel transmission coefficients for the incident and scattered beam, and $S_H(Q)$ is the

diffuse structural factor related to diffuse scattering at material inhomogeneities. For the sample deposited in vacuum, the average size of the nano-objects was around 1 nm, while by adding oxygen into the chamber of the growing film the average size slightly increased. The size distribution width is largest for 10 Pa and decreased with the oxygen pressure. The results of the fits are shown in Table III. The particles sizes are much smaller than the crystal sizes (about 20 nm), and can be ascribed to voids.

Table III. The average sizes of nano-voids, the width of size distribution of nano-voids, the real part of the refraction index δ (10^{-5}) and the corresponding density.

sample	Average size (nm)	Width (nm)	δ (10^{-5})	Density (g/cm^3)
vacuum	0.88	1.01	1.66	5.69
$10PaO_2$	0.93	2.12	1.620	5.56
$10PaO_2$/RF	1.01	2.22	1.633	5.60
30 Pa O_2	1.14	1.49	1.537	5.27
30 Pa O_2/RF	1.62	0.22	1.548	5.31
$70PaO_2$	1.62	0.07	1.464	5.02
70 Pa O_2/RF	1.71	0.01	1.489	5.11

For the samples deposited at pressures less than 70 Pa, interference maxima and minima can be seen (in the magnified part around the maximal intensity, Figure 5b), which correspond to those obtained by the reflectivity measurements plotted in Figure 3. The small variation of the position of the Yoneda maximum as a function of the oxygen pressure indicates different refraction indices and different densities for the examined films. A shift towards smaller Q_z values assumes a less dense material.

For the numerical calculation of the real part of the refraction index, $n = 1-\delta$, vertical cross sections close to the specular plane were fitted using equation 1 for the same grazing incidence angle as above, which corresponds to a penetration depth of some 50 nm. The obtained values for the real part of the refraction index (δ) and the corresponding densities are presented in Table III.

The density of the samples decreases with the oxygen pressure in the same way as the surface roughness increases. The average density decrease is partly a consequence of the surface roughness, and partly it is possibly due to an increase of the number of nano-

voids in the samples. The densities obtained with oxygen plasma are slightly higher than those obtained in oxygen atmosphere at the same pressures.

C. Surface morphology

1. AFM

AFM imaging provides information about the surface topology of the measured samples, as well as an estimate of the surface roughness. Figures 6a – c show representative AFM topography images, corresponding to the samples deposited at 10 Pa, 30 Pa and 30 Pa/RF, respectively. The imaged surfaces are not homogenous and flat, but show a granular structure. For each AFM image, we have performed a surface roughness analysis presented in Table IV. The surface roughness mostly follows the trend observed with XRR (Table II), where the roughness increases with the oxygen pressure, and also by applying RF excitation at the same pressure. However, there is a certain deviation in the surface roughness values acquired with AFM and those measured with XRR, where AFM gives around 3 to 6 times larger values. The observed discrepancy likely has more than one source. Namely, unlike XRR, which averages over a mm range, AFM is a local technique and thus is sensitive to local variations within the sample.
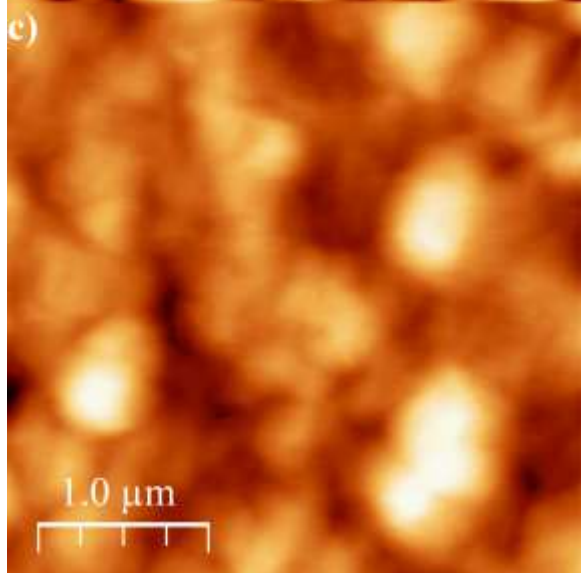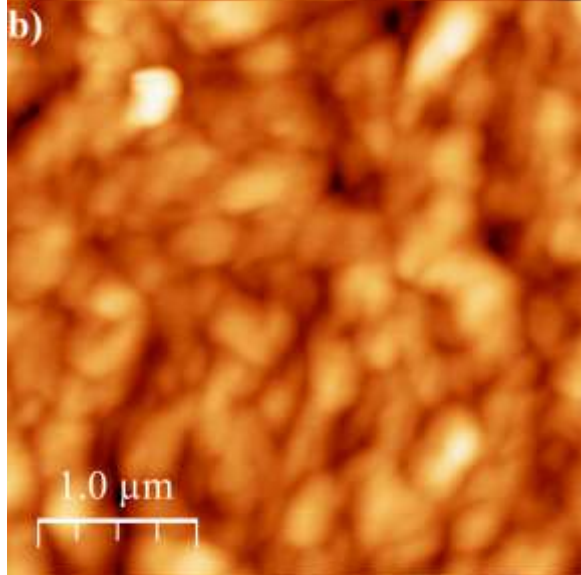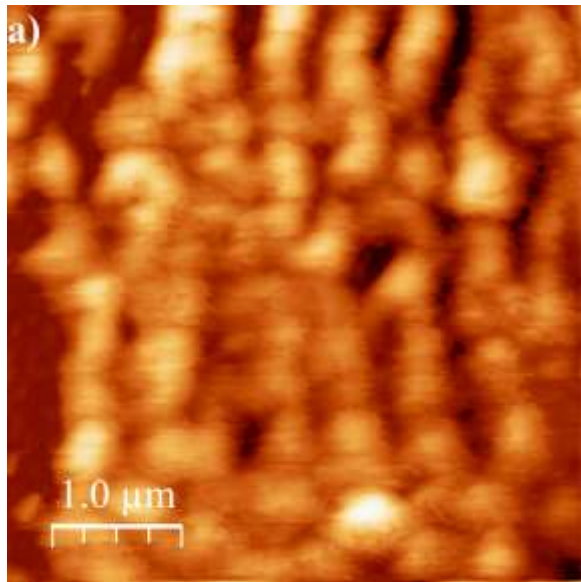
FIG. 6. (Color online) The AFM topographs of samples deposited under a) 10Pa O_2, b) 30 Pa O_2 and c) 30Pa O_2/RF.

Furthermore, as seen from the SEM micrographs (Figure 7), various larger particles are present on the surface, possibly as a consequence of droplet formation in the laser plume. These kinds of objects cause scattering of x-rays into larger angles and therefore do not contribute to the roughness calculation based on XRR data. On the contrary, such objects contribute to the roughness obtained from AFM.

Table IV. Surface roughness obtained from AFM topographs.

Sample	Roughness (nm) AFM
vacuum	16.5
10 Pa O_2	12.5
10 Pa O_2/ RF	15.8
30 Pa O_2	15.4
30 Pa O_2/RF	19
70 Pa O_2	21.1
70 Pa_O_2/ RF	21

2. FE-SEM

Characteristic FE-SEM micrographs are plotted in Figure 7, for samples deposited under 30Pa/RF and 70Pa/RF. The samples deposited under vacuum condition and at lower pressures, contain on the surface nanostructures with cylindrical shape, like these in Figure 7a and b, hollow at lower pressures, while solid at higher pressures. Also, the length of the cylinders was larger at higher pressures and RF excitation. A similar effect was already observed at PLD ZnO thin films deposited under various pressures [15]. At 70Pa, the cylindrical shapes turned to spherical. Such large objects are invisible for GISAXS and XRR.
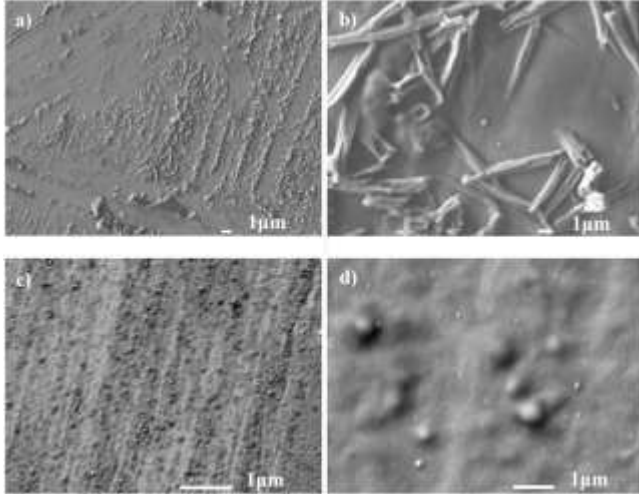
FIG. 7. (Color online) FESEM micrographs of samples deposited at 30 Pa O_2/RF (a, b) and 70 Pa O_2/RF (c, d).

D.   Photoluminescence

In Figure 8 the luminescence spectra normalized to the peak value of the UV band are plotted. All of them exhibit 3 well defined broad bands, around 3.3 eV (UV), 2.7eV (blue) and 1.9 eV (orange-red), while for samples deposited at 10 and 30 Pa oxygen there is in addition a weak shoulder at 3.15 eV (Figures 9a and 9b). The UV band is attributed to a band to band transition, while the others are defect related. The possible intrinsic defect centers in ZnO are (i) zinc vacancies (V_{Zn}), (ii) zinc on interstitial sites (Zn_i), (iii) oxygen on interstitial sites (O_i), and (iv) oxygen vacancies (V_O). The extrinsic defect in our samples appeared due to the Al dopand which is a shallow acceptor in ZnO and introduces an additional level close to the valence band. This level could shift and broaden the luminescence peaks. As seen from Figure 8a, a higher oxygen pressure during the deposition resulted in a change of the UV to defect bands ratio. The samples deposited under vacuum condition show similar intensities for the blue and UV bands, while the ratio of these peaks for the samples at 10 and 70 Pa slightly changes in favor of the UV peak. At 30 Pa the difference is substantial, and the UV peak is almost twice as high as the blue one. The red-orange peak is weak for all oxygen pressures. It shows that changing the oxygen pressure does not just have a simple influence on the film growth

18

through lowering the energy of the atoms emitted from the plasma plume towards the substrate. For samples deposited in RF oxygen plasma, Figure 8b, the ratio of the blue to UV peaks decreases gradually with pressure from 10Pa/RF towards 70Pa/RF. At the same time, the red-orange peak slightly increases with pressure and becomes considerably more intense for 70Pa/RF.

Recently, an increase of the luminescence peak was observed[29] in the red (655 nm, 1,89 eV) and, at the same time, a decrease of the blue-green peak (2.21-2.48 eV, 2.63 eV) by decreasing the crystal size of ZnO powder, by melting, from 240 to 80 nm. This effect was ascribed to an increase of the surface to bulk ratio, which favors surface defects. By an electron paramagnetic resonance (EPR) study, it was found that dominant surface defects were related to ionized oxygen vacancies, V_O^+, acting as deep donors. The dominant bulk defect, according to[29] should be singly ionized zinc vacancies, V_{Zn}^-, acting as shallow acceptors. This is consistent with theoretical calculations[30], which ascribe the blue luminescence to Zn vacancies. In some other experiments, the peak around 3 eV is also attributed to Zn vacancies[31]. In our experiment, both peaks are present and due to the excess of oxygen in the atmosphere of the growing film such intrinsic defects are expected. Moreover, the shoulder around 3 eV disappears with decreasing intensity of the blue peak (Figures 9a and b).

The red luminescence is usually present in experiments with excess of oxygen, while it is mostly attributed to oxygen interstitials, O_i[32-34]. It is interesting to note that this peak is unexpectedly weak for our samples, except for that made at 70Pa O_2/RF.

These attributions are consistent with the results plotted in Figures 8 and 9. For samples deposited at higher pressure and by RF excitation, the surface roughness is larger, which implies a larger surface-to-bulk ratio on top of the samples. Also, the peak attributed to surface defects, presumably O_i or V_O^+, increases for 30 Pa/RF and becomes dominant at 70Pa/RF.

In Figure 9, the difference between samples deposited in neutral oxygen atmosphere and in RF excited oxygen atmosphere is clearly seen. The RF introduces additional active oxygen species, which results in more oxygen related defects, and hence a higher red luminescence. At the same time the blue luminescence decreases, indicating

19

a lower density of Zn vacancies. Furthermore, the luminescence peak related to the band-to-band transition becomes narrower for samples deposited in RF plasma atmosphere and better defined, indicating an improvement of the crystal structure, which is consistent with a decreasing density of "bulk" defects. Since our samples have a granular structure (Figure 7), and the nanovoids became larger with increasing oxygen pressure and RF excitation (Table III), the excess of oxygen atoms estimated from ERDA measurements (Table I) are most probably located on the surface of the film, and at the grain boundaries as well.
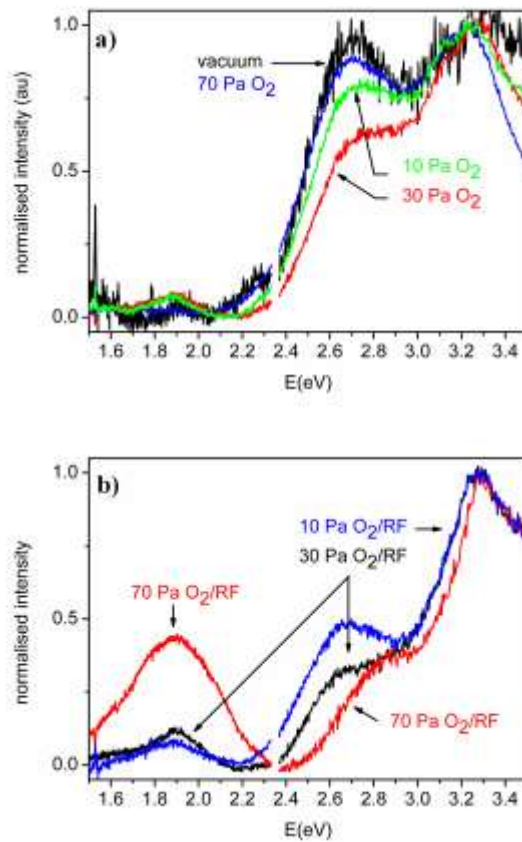

FIG. 8. (Color online) Normalized luminescence intensities for samples deposited under various oxygen pressures in a) neutral atmosphere and b) with RF excitation.
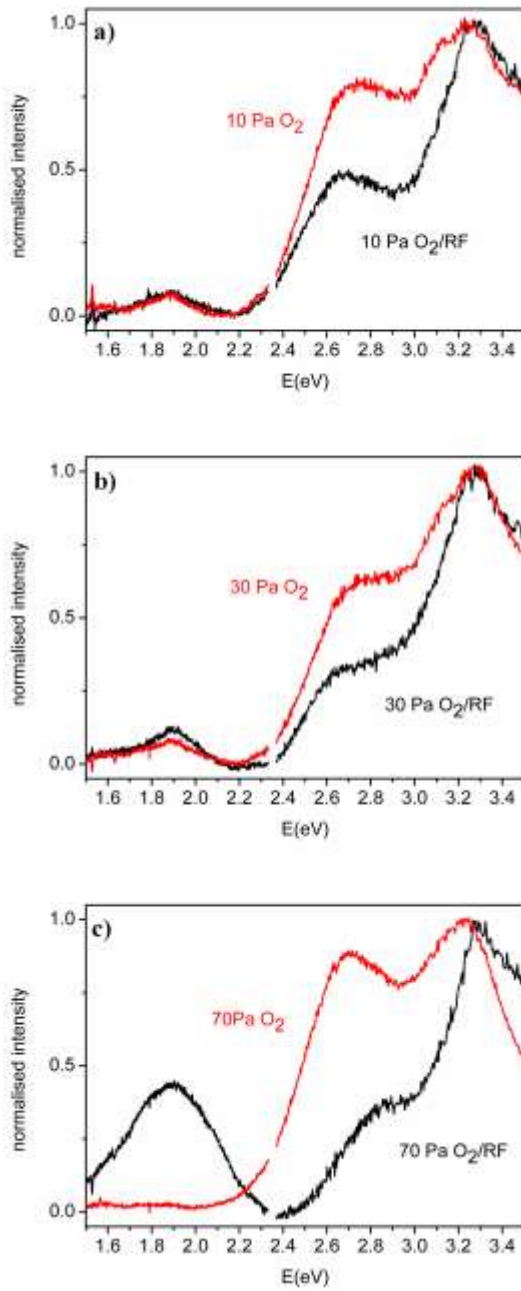
FIG.9. (Color online) Normalized luminescence intensities for samples deposited in neutral and RF excited oxygen atmosphere for various pressures a) 10Pa, b) 30Pa and c) 70 Pa.

E. Discussion

The main structural properties related to the atmosphere between a laser plume and a growing film are an increase of the surface roughness and a decrease of the sample density with increasing oxygen pressure during the deposition. The RF excitation does not change a lot in the crystallites orientation and size, but influences the point defects formation and annihilation. An increase of the pressure decreases the mean free path of particles emitted from the target towards the substrate, and hence lowers the energy of the particles which build the film, due to collisions with gas. A lower energy of the incoming particles means they have a lower surface mobility and lower energy transfer from the laser plume to the growing film, and hence the substrate temperature is also lower. The final effect is that the energy of those particles which build the film becomes too low for a particle to find the place with minimum energy and to form the perfect homogeneous layer.

For a typical PLD deposition, used also in this study, the laser pulse rate is several Hz and the target to substrate distance is a few cm. Since the velocity of the emitted particles from the laser plume is above 10^6 cm/s, all of them reach the substrate and condense well before the next laser shot, and thus the film does not grow continuously. The samples of about 100-200 nm thickness were deposited within 2000 pulses, which means that the growing rate was about 10 pulses for one monolayer. That is why the atmosphere between target and substrate has a substantial influence on the chemistry of film growth not only during each pulse but also between pulses. Chemical reactions between oxygen and growing film are expected to be more pronounced in the case of using plasma instead of neutral gas. The presented results show that the addition of RF excitation, e.g. the increase of oxygen reactivity due to active oxygen species (O and probably O_2* as well) lowers the defect density and changes the intensity ratio between defect related and band to band related luminescence peaks. The influence of the RF excitation depends on the exact plasma condition. The combination of RF power, pressure and position with respect to the growing film determinates the density and nature of the excited oxygen particles, and their influence cannot be predicted without a proper measurement of the RF plasma properties. For this experiment, the concentration of atomic oxygen did not change too much in the applied pressure range, but according to

the literature the concentration of O_2* could change by several orders of magnitude[35]. In addition, the laser plasma plume contains also ionized particles and their spatial distribution changes with the oxygen pressure.

However, this work demonstrates the additional possibility of adjusting the structural and optical properties of ZnO thin films deposited by PLD, and promotes the method itself.

IV. SUMMARY AND CONCLUSIONS

Nano-crystalline ZnO thin films were deposited by pulsed laser deposition in oxygen and RF excited oxygen atmosphere under various pressures. By analyzing GISAXS, GIXRD, XRR and ERDA data it was found that the roughness of film surfaces increases with increasing gas pressure, and the density decreases due to the formation of nano-voids. This effect was ascribed to a lowering of the energy of the atoms which build the films, due to an increased number of collisions on the way from the target to the growing film. Particles with too low energy for surface migration do not find the optimal place for smooth layer growth. The rough surface results in a larger surface to bulk ratio, which favors surface defects compared to bulk ones. Both effects are evident from the luminescence spectra. A pressure increase during deposition had as a consequence a narrowing of the UV-peak, indicating a more relaxed structure. In the same time, the blue peak intensity decreases supporting its attribution to Zn_i defects. The accompanied slight increase of the red-luminescence peak appeared due to the increase of the surface roughness and surfaces of nano-voids in the material.

The addition of excited oxygen particles from a RF plasma improves the structural ordering by lowering the defect level, which is evident from GISAXS and luminescence measurements. This effect depends on the total oxygen pressure, e.g. on the nature and concentration of excited particles, and thus that needs to be measured for proper modelling. This is why the RF plasma monitoring is strongly desired in order to control and tailor the properties of deposited films.

ACKNOWLEDGMENTS

[1] K. Keis, C. Bauer, G. Boschloo, A. Hagfeldt, K. Westermark, H. Rensmo, and H. Siegbahn, J. Photochem. Photobiol. A **148**, 57-64 (2002).

[2] B. Weintraub, Z. Zhou, Y. Li, and Y. Deng, Nanoscale **2**, 1573-1587 (2010).

[3] X.W. Sun, J.Z. Huang, J.X. Wang, and Z. Xu, Nano Lett. **8**, 1219-1223 (2008).

[4] C.S. Rout, and C.N.R. Rao, Nanotechnology **19**,285203 (2008).

[5] J.M. Wu, Y.-R. Chen, and Y.-H. Lin, Nanoscale **3**, 1053-1058 (2011).

[6] H. Lu, L. Liao, J. Li, D. Wang, H. He, Q. Fu, L. Xu, and Y. Tian, J. Phys. Chem. **23**,23211-23214 (2006).

[7] K. Liu, M. Sakurai, and M. Aono, Sensors **10**, 8604-8634(2010).

[8] A.B. Djurišić, and Y.H. Leung,Small **2**, 944-961(2006).

[9] N. Krstulović, N. Čutić, and S. Milošević, Spectrochim. Acta B **63**, 1233–1239(2008).

[10] N. Krstulović, I. Labazan, and S. Milošević, Phys. J. D **37**, 209–215(2006).

[11] I. Labazan, N. Krstulović, and S. Milošević,Chem. Phys. Lett. **428**, 13–17(2006).

[12] I. Labazan, N. Krstulović, and S. Milošević, J. Phys. D: Appl. Phys. **36**, 2465–2470(2003).

[13] P. Dubček, B. Pivac, S. Milošević, N. Krstulović, Z. Kregar, and S. Bernstorff, Appl. Surf. Sci.**257**, 5358–5361(2011).

[14] P. Dubček, B. Pivac, S. Milošević, N. Krstulović, Z. Kregar, and S. Bernstorff, ISRN Nanomaterials **2013**, 1-13(2013).

[15] R. Kumar, G. Kumar, and A. Umar, J. Nanosci. Nanotechnol. **14**, 1911-1930(2014).

[16] A. Aravind, M.K. Jayaraj, M. Kumar, and R. Chandra, Appl. Surf. Sci. **286**, 54-60(2013).

[17]W. Zhaoyang, and H. Lizhong, Vacuum **83**, 906-909(2009).

[18]J.-W. Park, M.-S. Oh, S.-J. Park, and Y.Yoo, J. Nanoelectron. Optoe. **9**, 162-166(2014).

[19]S.-H. Huang, Y.-C. Chou, C.-M. Chou, and V.K.S. Hsiao, Appl. Surf. Sci. **266**, 194-198(2013).

[20]D. Vujosevic, M. Mozetic, U. Cvelbar, N. Krstulovic, and S. Milosevic, J. Appl. Phys. **101**, 103305-1-7(2007).

[21]H. Amenitsch, S. Bernstorff, and P. Laggner, Rev. Sci. Instrum. **66**, 1624-1626(1995).

[22]I. Horcas, R. Fernández, J.M. Gómez-Rodríguez, J. Colchero, J. Gómez-Herrero, and A.M. Baro, Rev SciInstrum. **78**, 13705-0(2007).

[23]Z. Siketic, I. BogdanovicRadovic, and M. Jaksic, Nucl. Instrum. Meth B **266**, 1328-1332(2008).

[24]D. Gracin, K. Juraić, and I. BogdanovićRadović, Vacuum **80**, 146-150(2005).

[25]K. Salamon, O. Milat, N. Radić, P. Dubček, M. Jerčinović, and S. Bernstorff,J. Phys. D: Appl. Phys. **46**, 095304-1-10(2013).

[26]L. G. Parratt, Phys. Rev. **95**,359-369 (1954).

[27]L. Nevot, and P. Croce, Rev. Phys. Appl. **15**,761-779(1980).

[28]G. Renaud, R. Lazzari, and F. Leroy, Surf. Sci. Rep. **64**, 255-380(2009).

[29]H. Kaftelen, K. Ocakoglu, R. Thomann, S. Tu, S. Weber, and E. Erdem, Phys. Rev. B **86**, 014113-1-9(2012).

[30]P.S. Xu, Y.M. Sun, C. S. Shi, F.Q. Xu, and H.B. Pan, Nucl. Instrum. Meth. B **199**, 286-290(2003).

[31]D. Zhao, C. Andreazza, P. Andreazza, J. Ma, Y. Liu, and D. Shen, Chem. Phys. Lett. **399**, 522-526(2004).

[32]X. Liu, X. Wu, H. Cao, and R.P.H. Chang, J. Appl. Phys. **95**, 3141(2004).

[33]R.B.M. Cross, M.M. De Souza, and E.M. Sankara Narayanan,Nanotechnology **16**, 2188-2192(2005).

[34]W.M. Kwok, Y.H. Leung, A.B. Djurisic, W.K. Chan, and D.L. Phillips, Appl. Phys. Lett. **87**, 093108 -1-3(2005).

[35]S. Rajendiran, A.K. Rossall, A. Gibson, andE.Wagenaars, Surf. Coat. Tech. **260**, 417–423(2014).

(100) (002) (101) (102) (110) (103) (112)

ZnO powder

70 Pa O$_2$

30 Pa O$_2$

10 Pa O$_2$

vacuum

Intensity (a.u.)

2Θ (deg)

- 70 Pa O$_2$/RF
- 70 Pa O$_2$
- 30 Pa O$_2$/RF
- 30 Pa O$_2$
- 10 Pa O$_2$/RF
- 10 Pa O$_2$
- vacuum

Reflectivity (a.u.)

α_i (deg)

a)

70 Pa O$_2$/RF
70 Pa O$_2$
30 Pa O$_2$/RF
30 Pa O$_2$
10 Pa O$_2$/RF
10 Pa O$_2$
vacuum

b)

70 Pa O$_2$/RF
70 Pa O$_2$
30 Pa O$_2$/RF
30 Pa O$_2$
10 Pa O$_2$/RF
10 Pa O$_2$
vacuum

a)

1.0 μm

b)

1.0 μm

c)

1.0 μm

a)

normalised intensity (au)

vacuum
70 Pa O$_2$
10 Pa O$_2$
30 Pa O$_2$

E(eV)

b)

normalised intensity

70 Pa O$_2$/RF
10 Pa O$_2$/RF
30 Pa O$_2$/RF
70 Pa O$_2$/RF

E(eV)